Research Article

For reprint orders, please contact: reprints@futuremedicine.com

Nanomedicine

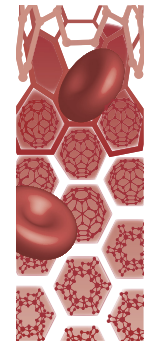

Metallated porphyrin-doped conjugated polymer nanoparticles for efficient photodynamic therapy of brain and colorectal tumor cells

Luis Exequiel Ibarra[1], Gabriela Valeria Porcal[‡,2,3], Lorena Paola Macor[‡,2,3], Rodrigo Andrés Ponzio[3,4], Ramiro Martin Spada[2,3], Carolina Lorente[5], Carlos Alberto Chesta[*,2,3], Viviana Alicia Rivarola[**,1] & Rodrigo Emiliano Palacios[***,2,3]

[1]Universidad Nacional de Río Cuarto y CONICET, Instituto de Biotecnología Ambiental y Salud (INBIAS), Dto. Biología Molecular, Facultad de Ciencias Exactas Fisicoquímicas y Naturales, Río Cuarto (5800), Córdoba, Argentina

[2]Universidad Nacional de Río Cuarto y CONICET, Dto. Química, Facultad de Ciencias Exactas Fisicoquímicas y Naturales, Río Cuarto (5800), Córdoba, Argentina

[3]Instituto de Investigaciones en Tecnologías Energéticas y Materiales Avanzados (IITEMA), UNRC-CONICET, Argentina

[4]Universidad Nacional de Río Cuarto y CONICET, Dto. Física, Facultad de Ciencias Exactas Fisicoquímicas y Naturales, Río Cuarto (5800), Córdoba, Argentina

[5]Universidad Nacional de La Plata y CONICET, Instituto de Investigaciones Fisicoquímicas Teóricas y Aplicadas (INIFTA), Dto. Química, Facultad de Ciencias Exactas, CCT La Plata CONICET, La Plata (1900), Buenos Aires, Argentina

[*]Author for correspondence: cchesta@exa.unrc.edu.ar

[**]Author for correspondence: vrivarola@exa.unrc.edu.ar

*** Author for correspondence: rpalacios@exa.unrc.edu.ar

[‡] Authors contributed equally

Aim: Assess biocompatibility, uptake and photodynamic therapy (PDT) mechanism of metallated porphyrin doped conjugated polymer nanoparticles (CPNs) in human brain and colorectal tumor cells and macrophages. **Materials & methods:** CPNs were developed employing 9,9-dioctylfluorene-*alt*-benzothiadiazole, an amphiphilic polymer (PS-PEG-COOH), and platinum octaethylporphyrin. T98G, SW480 and RAW 264.7 cell lines were exposed to CPNs to assess uptake and intracellular localization. Additionally, a PDT protocol using CPNs was employed for the *in vitro* killing of cancer and macrophage cell lines. **Results & conclusion:** CPNs were well incorporated into glioblastoma and macrophage cells with localization in lysosomes. SW480 cells were less efficient incorporating CPNs with localization in the plasma membrane. In all cell lines PDT treatment was efficient inducing oxidative stress that triggered apoptosis.

First draft submitted: 21 September 2017; Accepted for publication: 8 January 2018; Published online: 29 January 2018

Keywords: apoptosis • brain tumor • colorectal tumor • conjugated polymer nanoparticles • metallated porphyrin • photodynamic therapy • ROS

Photodynamic therapy (PDT) is based on a phenomenon known as photodynamic action, which is a term used to describe the damage to living tissue caused by photosensitizers (PS) in the presence of visible light and oxygen. This therapy has received a great attention in cancer research and, *a priori*, all solid tumors that are accessible to the PS and optical radiation are amenable for the implementation of PDT [1–3]. Recently, PDT has been recognized as a viable therapy for treatment of brain tumors. Unlike surgery and high-energy radiation, PDT can selectively treat areas of micro-invasion and simultaneously spare sensitive brain regions due to selective location of the PS in cancerous tissue [4–6]. This advantage over conventional therapy may improve treatment outcome in patients whose survival is overall quite poor after traditional treatments [7,8]. On the other hand, colorectal cancer (CRC) is worldwide the third most common cancer in men and the second in women. Thus, new and efficient CRC treatments are currently in high demand by the medical community. Endoscopic application of PDT is specially well suited for the treatment of CRC; in particular in precancerous lesions and even in advanced tumors demonstrating significant advantages over current therapy [9,10].

Future Medicine

In short, PDT involves the administration of a tumor-localizing PS followed by local irradiation of the tumor with light of the appropriated wavelength to activate the PS. The excited PS (PS*) can generate several of cytotoxic reactive oxygen species (ROS), among them singlet oxygen ($O_2(^1\Delta_g)$), through different mechanisms [2,11–14]. However, the photosensitized generation of $O_2(^1\Delta_g)$ is preferred over that of other ROS in their application to PDT, particularly because the PS it is not consumed during the process. A major advantage of PDT over conventional treatments is that the PS is intrinsically minimally toxic in the absence of light and hence, PS accumulation in nonspecific tissues results in negligible systemic toxicity. Furthermore, the activating light is non-ionizing and thus, its effect on tissues without the PS is not harmful. Accordingly, PDT has the potential to be repeated safely, if needed, with minimum risk of harming neighboring healthy tissue [15].

A wide range of PS has been evaluated so far and only a few PS have successfully transitioned from bench to bedside applications [15,16]. A good PS must have negligible dark-toxicity, high quantum yield of $O_2(^1\Delta_g)$ (Φ_Δ) and good photostability.

Owing to their large π-conjugated backbones and delocalized electronic structure, conjugated polymers (CPs) have been widely applied in optoelectronic devices, such as light-emitting diodes, photovoltaic cells and field effect transistors [17–21]. The excellent light-collection and energy transfer properties of CPs make them particularly attractive for the generation of multifunctional nanoparticles in theragnosis anticancer drug development [22–25]. In particular, nanoparticles based on conjugated polymer nanoparticles (CPNs) are promising alternatives for this purpose due to its tunable photoemission, high brightness, low cytotoxicity, excellent photostability and simple preparation [20,26–29]. Previous studies indicate that CPNs under light irradiation produce ROS that can kill bacteria and tumor cells [30–33]. In comparison to conventional organic molecule PS, the advantages of CPNs for ROS generation lies in the extraordinarily large one-photon (visible range) and two-photon (NIR) excitation cross-sections of CPs and its efficient energy transfer to dopants. This 'antenna' effect results in an amplified capacity to generate the PS* and thus to generate $O_2(^1\Delta_g)$ making possible the implementation of PDT protocols with both low PS and light doses. Additionally, these CPNs can be easily biofunctionalized to enhance their selectivity toward cancerous tissue [34–37].

In this study, CPNs were synthesized employing the conjugated polymer poly(9,9-dioctylfluorene-*alt*-benzothiadiazole) (F8BT) and an amphiphilic copolymer stabilizer (PS-PEG-COOH) to achieve colloidal stability in high ionic strength aqueous media, including physiological media. An organic hydrophobic porphyrin: platinum octaethylporphyrin (PtOEP) was incorporated into the CPNs to improve its ability to generate $O_2(^1\Delta_g)$. A similar strategy to enhance $O_2(^1\Delta_g)$ production by CPNs has been previously reported by different authors [32–34,36,38]. Our CPNs were extensively photophysical/photochemically characterized and their degree of cell incorporation, cytotoxicity and PDT efficiency were tested in glioblastoma (T98G), colorectal adenocarcinoma (SW480) and macrophage (RAW 264.7). Our findings provide new information regarding PDT protocol and cellular damage mechanisms of CPNs in cancerous diseases positioning these nanoparticles as promising PS for therapeutic use. A schematic overview of our approach is presented in Figure 1.

Materials & methods

Materials

3-[10-(2-Carboxyethyl)anthracen-9-yl]propanoic acid (ADPA, 99%, Sigma-Aldrich, MO, USA) was used as received. Tetrahydrofuran (THF, HPLC grade, Cicarelli) was refluxed for 5 h with potassium hydroxide pellets (KOH, pro-analysis grade, Taurus) and subsequently distilled over freshly activated molecular sieves (4 Å, Sigma-Aldrich). Double-distill water was further purified by an ELGA PURELAB Classic UV system (~18.2 MΩ/cm) to remove ions, organic and particulate matter (0.2 μm filter). The fluorescent semiconductor polymer poly(9,9-dioctylfluorene-*alt*-benzothiadiazole) (F8BT, Mn = 70,000 g/mol, PDI = 2.4, ADS Inc., Canada), the comb-like polymer, polystyrene grafted with ethylene oxide functionalized with carboxyl groups (PS-PEG-COOH, back bone Mn = 6500 g/mol, branches of Mn = 4600 g/mol, Polymer Source Inc, Canada), the porphyrin Pt(II) octaethylporphyrin (PtOEP, >95%, Frontier Scientific, UT, USA), and argon (Ar, 99.998 %, Linde, Buenos Aires, Argentina) were used as received. Dulbecco's modified Eagle's medium (DMEM, Gibco®), Penicillin 10,000 units/ml—streptomycin 10,000 μg/ml solution Gibco®, glutamine (GlutaMAXTM 100X Gibco®), trypsin-EDTA Solution 10 × Gibco®, sodium pyruvate 100 mM solution Gibco®, phosphate buffered saline (PBS) buffer solution, LysoTracker® Red, MitoTracker® Red CMXRos and Rhodamine Phalloidin (Molecular Probes™) were purchased from Life Technologies (NY, USA). Fetal bovine serum (FBS) was purchased from Internegocios S.A (Buenos Aires, Argentina). Fluoromount™, 3-(4,5-dimethylthiazol-2-yl)-2,5-diphenyl tetra-

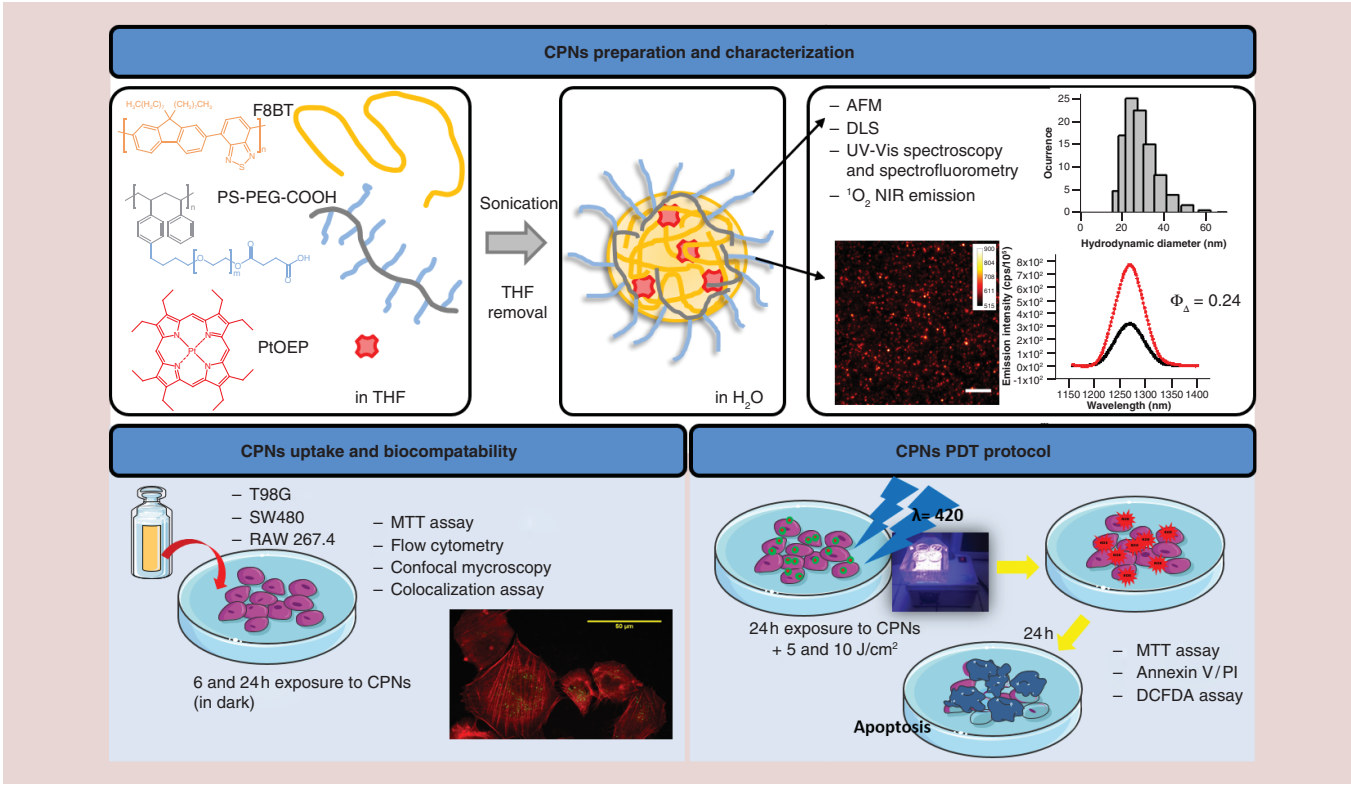

Figure 1. Schematic representation of CPNs preparation and *in vitro* studies.

zoliumbromide) (MTT), 2′,7′-dichlorodihydrofluorescein diacetate (DCFH-DA, ≥97%) and FITC Annexin V Apoptosis Detection Kit II were purchase from Sigma-Aldrich.

Particle synthesis

F8BT was dissolved (with the aid of sonication and mild heating ~40°C) in freshly distilled THF to a concentration slightly above 500 mg/l. The solution was filtered with a 0.2 µm pore-size PTFE membrane syringe filter (Iso-Disc, Sigma-Aldrich) to remove any undissolved polymer. The concentration of the filtered solution was recalculated by comparing absorption spectra before and after filtration, and the resulting solution was diluted to a final concentration of 500 mg/l. On the other hand, stock solutions of PS-PEG-COOH (2000 mg/l) and PtOETP (250 mg/l) in THF were prepared independently. Next, all solutions were mixed and diluted in THF to a final concentration of 50, 10 and 5 mg/l for F8BT, PS-PEG-COOH and PtOEP, respectively. Doped CPNs functionalized with PS-PEG-COOH in aqueous solution were prepared by the nanoprecipitation method. Briefly, 5 ml of the F8BT/PS-PEG-COOH/PtOEP solution in THF was quickly added to 10 ml of H_2O while sonicating (Arcano, PS-30A). Later, THF and H_2O were removed under reduced pressure (using a rotary evaporator) yielding a final volume of 5 ml. Finally, the produced particle dispersion was filtered through a 0.2 µm filter to eliminate large aggregates. The concentration of F8BT and PtOEP in the resulting filtered solution was recalculated by comparing absorption spectra before and after filtration. The proportion of the CPNs components is assumed to be maintained after filtration. Unless otherwise noted, the given CPNs concentrations are expressed in terms of F8BT mass concentration.

Characterization techniques

Steady state absorption & emission

UV–Vis absorption spectra were recorded on a diode-array spectrophotometer (Agilent Hewlett-Packard, HP 8452A) in 1 cm cuvettes at room temperature. Emission measurements were acquired from dilute solutions (Abs_{max} <0.1) in 1 cm cuvettes at room temperature and with excitation at the sample absorption maximum. Corrected emission spectra were recorded with a spectrofluorometer (Horiba, Fluoromax-4). Steady-state singlet

10.2217/nnm-2017-0292

oxygen phosphorescence measurements were carried-out using a NIR PMT Module H10330–45 (Hamamatsu) coupled to a single-photon-counting equipment FL3 TCSPC-SP (Horiba Jobin Yvon) fitted with a Xe (CW 450 W) lamp, excitation (FL-1004 with a 1200 groove per mm, 330 nm blaze grating) and emission (FL-1004 with a 600 groove per mm, 1000 nm blaze grating) monochromators. Absorbance of CPNs samples and reference (Eosin Y, $\Phi_\Delta = 0.58$ in D_2O) [39] were matched at 487 nm and $O_2(^1\Delta_g)$ phosphorescence was detected at 90° with respect to the excitation beam. Corrected emission spectra obtained with excitation at 487 nm were recorded between 950 and 1400 nm and the total integrated phosphorescence intensities were calculated by integrating the emission band centered at 1268 nm. All experiments were performed in D_2O at room temperature.

Photooxidation assays of ADPA

Photooxidation experiments were conducted by placing solutions of ADPA in water suspensions of CPNs inside a fluorescence cuvette. It is well known that anthracene derivatives with substituents in the 9 and 10 position, such as ADPA, react efficiently with $O_2(^1\Delta_g)$ to form the corresponding endoperoxides (ADPA-O_2) [40]. Samples were irradiated with two blue LEDs (λ_{ext} ~467 nm, FWHM ~28 nm, total optical power ~14 mW) while simultaneously monitoring the changes in absorbance of ADPA as function of time. It is important to note that the LEDs sources selectively excite CPNs and do not photoexcite ADPA. Absorption spectra of the solutions were automatically collected at constant time intervals using a UV–Vis spectrophotometer equipped with a kinetic software module. The extinction coefficient of the endoperoxide, ADPA-O_2, in water at 400 nm is considered to be negligible as compared with that of ADPA [41]. Thus, the oxidation reaction (ADPA + $O_2(^1\Delta_g) \rightarrow$ ADPA-O_2) is conveniently followed by monitoring changes in absorption at 400 nm and directly assigning these changes to variations in ADPA concentration. Kinetic traces were constructed by monitoring the absorption at the previously mentioned wavelength as a function of photoirradiation time (t), each absorption value was first corrected by subtracting the initial absorption of the sensitizing CPNs at the same wavelength and the resulting values were later normalized to the absorption at t = 0 s (A_0) and plotted as (A/A_0) versus t. Control experiments in absence of substrate showed that the absorption of CPNs sensitizers at the measured wavelength remains constant through the irradiation time. During measurements, ADPA solutions were continuously stirred and open to the atmosphere. For these experiments, the initial concentrations of CPNs sensitizers and ADPA were 6.6 mg/l and 33 μM, respectively.

Dynamic light scattering

Measurements were performed with a Zeta-Sizer Nano ZS90 Instrument at 25°C. Light scattering results were analyzed with Zetasizer software (provided by the instrument manufacturer) to obtain hydrodynamic radius distributions by number. Particle suspensions for dynamic light scattering (DLS) were prepared with water filtered through 0.2 μm pore filters right before data acquisition. Extreme care was taken to reduce contamination by dust.

Atomic force microscopy

Samples were prepared by spincasting particle suspensions (10.7 mg/l) on freshly cleaved mica substrates (SPI, Grade V-1 Muscovite). Atomic force microscopy (AFM) images were obtained on an Agilent 5400 AFM microscope in tapping mode operating at a scan rate of 12.05 μm/s, with resolution of 512 × 512 pixels and a physical image size of 15 × 15 μm, using a cantilever (μMasch, NSC15/AIBS) with nominal frequency of vibration of 325 kHz, radius of curvature <10 nm and force constant of 46 N/m. Images (~10 images per sample for a total of ~300 particles) were processed with the Gwyddion software [42]. Field curvature effects were first corrected using the 'Remove Polynomial Background', 'Correct lines by matching height median' and 'Level data by mean plane subtraction' functions. The resulting images were then analyzed, with the same software, to select particles using the 'Mark grains by threshold' function and finally the 'Grain Distributions' function was used to obtain the maximum height of each identified particle. The resulting data were used to build particle height histograms.

Cellular assays

Cell culture

T98G (ATCC® CRL-1690™; human glioblastoma multiforme), SW480 (ATCC CCL-228™) (human Dukes' type B, colorectal adenocarcinoma) and RAW 264.7 (ATCC TIB-71™) (mouse macrophages) were grown in DMEM medium supplemented with 10% v/v FBS, 1% v/v glutamine (GlutaMAXTM 100X), 1% v/v antibiotic (Penicillin 10,000 units/ml – streptomycin 10,000 μg/ml) and 1% v/v of sodium pyruvate 100 mM at 37°C in a humidified and 5% CO_2 atmosphere (Hera Cell, Thermo Scientific, MA, USA).

Cell incubation with CPNs for fluorescence imaging

T98G, SW480 and RAW 264.7 cell lines were seeded (10^5 cells/ml) on glass-coverslips placed within 35 mm culture dishes and then incubated overnight in 2 ml of DMEM containing 10% FBS at 37°C to 70–80% confluency. Afterward, the media was removed and cells were washed with PBS and incubated with 2 ml of DMEM containing 10% FBS and ~12 mg/l CPNs. After 24 h, CPNs solution was removed and cells were washed with PBS. Later, cells were incubated with LysoTracker Red or MitoTracker Red CMXRos according manufacturer's protocols (Molecular Probes) for co-localization assays. Finally, cells were fixed (10 min in 4% (w/v) paraformaldehyde in PBS) and glass coverslips containing cells were mounted over slides in aqueous based mounting medium Fluoromount in order to improve the quality of images obtained. Filaments of actin corresponding to the cytoskeleton were stained for 20 min with Rhodamine Phalloidin (Molecular Probes) after fixing of the cells.

CPNs fluorescence imaging

Fluorescence micrographs of single particles were measured in a home-made EPI-fluorescence microscope that has been previously described in detail [43] and that was operated in TIRF mode. Samples were prepared by deposition of CPNs suspensions in water on clean glass coverslip substrates through spincasting. Excitation was provided by the 458 nm line of a CW Ar-Ion laser (Modu-Laser, Stellar Pro L 300). The laser beam was magnified ten-times using a pair of lenses (Thorlabs, LA1540-A-ML and Thorlabs, AC254–150-A-ML) and focused with a third lens (Thorlabs, LA1979-A, mounted over a micrometer driven translation stage) at the back focal plane of a 60 × 1.49 NA objective (Nikon, CFI Apo TIRF Oil immersion) previous reflection on a dichroic mirror (Edmund #86–331). The focused beam was displaced from the objective optical axis by moving the focusing lens until the TIRF condition was achieved at the coverslip-sample interface. Emission from the sample was collected through the same objective, spectrally filtered with a long pass filter (Semrock BLP01–458R-25), and focused with a tube lens (Nikon, ITL200 # Thorlabs) on the chip of an EM-CCD camera (Andor, iXonEM + 897) to form fluorescence micrographs images which were recorded using Andor Solis software. For intracellular localization of CPNs the fixed cells were examined with an Olympus FV1200 Laser Scanning confocal microscope. Confocal fluorescence images of cells with selective detection of CPNs (green emission), mitochondrias (MitoTracker Red CMXRos, red emission), lysosomes (LysoTracker Red, red emission) and actin filaments (Rhodamine Phalloidin, red emission) were overlaid (merged) using ImageJ (NHI) software. Regions of interest were hand-drawn on merged images to select individual cells and colocalization analysis was performed, over different subcellular planes, using Fiji's plugin Coloc 2 [44,45]. Additionally, for SW480 cells, confocal reflection images were also collected and overlaid with confocal fluorescence images.

Quantification of CPNs incorporation using flow cytometry

T98G, SW480 and RAW 264.7 at 10^5 cells/ml concentration were incubated with 24 mg/l CPNs in medium supplemented with 10 % FBS for 24 h. Then the cells were harvested, washed with PBS, resuspended in PBS supplemented with 1 % of FBS and particle incorporation was studied on these samples using flow cytometry (BD FACS Canto II, BD Biosciences, CA, USA). Cells of the three lines without CPNs were employed as control. A total of two replicas were performed and the data were processed with FlowJo software (provided by the equipment's manufacturer). The cells that incorporated CPNs were identified in the green channel (523/30 nm) starting from the intersection of the histograms of control cells and cells incubated with nanoparticles.

Biocompatibility of CPNs in macrophages & tumor cells

Cytotoxicity was tested following the EN ISO 10993–5 protocol. T98G, SW480 and RAW 264.7 cells were seeded into 96-well microplates at a concentration of 10^5 cells/ml and allowed to grow for 24 h to a subconfluent state (80% confluency). The culture medium was replaced with fresh medium supplemented with 10% FBS having different CPNs concentrations (3, 6, 12 and 24 mg/l) and samples were incubated for 24 and 48 h with 100 µl of tested suspensions. CPNs suspensions were removed and 50 µl of MTT solution (1 mg/ml in culture medium) was added and cells were incubated for 2 h at 37°C in 5% CO_2 prior to the analysis. Thereafter, the medium was removed and 100 µl of DMSO was added to dissolve blue formazan crystals. The absorbance of the formed dye was measured at 570 nm using a microplate reader. Absorbance values for untreated wells were taken as control (100% survival). All samples were kept in the dark during CPNs uptake and MTT assays.

10.2217/nnm-2017-0292

Photodynamic treatment with CPNs

For PDT experiments PS incubation and MTT viability assays were performed following the EN ISO 10993–5 protocol. To evaluate the PDT effect of CPNs, cell lines were incubated with different concentrations of CPNs (3, 6, 12 and 24 mg/l) in DMEM with 10 % FBS for 24 h. After removing the medium, cells were washed twice with PBS to eliminate free nanoparticles (not incorporated to cells) and fresh medium was added. Then, cells were irradiated with a MultiLED system (420 ± 17 nm). The irradiance (flux density) on the cell monolayer was 50 mW/cm^2 (as measured by a Laser Mate-Q radiometer, Coherent) and two light doses (radiant exposures) were used (5 and 10 J/cm^2). The PDT effect of CPNs was evaluated 24 h after treatment by determining cell viability (MTT assay, *vide supra*) and by observation of cell's morphological changes (using brightfield microscopy, in a Nikon Eclipse Ti-S microscope equipped with a LWD 20x/0.4 objective lens and a Nikon DS-QiMC CCD camera). Additionally the number of live cells 6 and 24 h after PDT treatment was determined using fluorescence staining (FITC Annexin V Apoptosis Detection Kit II) and flow cytometry (*vide infra*). Three independent PDT experiments were performed (with n = 6 for each experiment).

Determination of oxidative stress

Intracellular oxidative stress produced upon CPNs photoirradiation was measured using the fluorescent molecular probe DCFH-DA. This probe easily penetrates cell membranes and it is enzymatically hydrolyzed by intracellular esterases to form the nonpermeable DCFH. This hydrolyzed nonfluorescent compound after oxidation by peroxide species gives rise to a strong green fluorescent molecule [46]. Cell lines were first incubated with CPNs (24 mg/l) for 24 h and washed twice with PBS. Later, cells were incubated with DCFH-DA for 30 min, irradiated with a 10 J/cm^2, washed with PBS and kept in PBS for imaging. Finally, cells were observed in an epiluminescence microscope (Nikon Eclipse Ti-S equipped with a LWD 40X/0.55 objective and DS-QiMC CCD camera). Three negative control experiments were performed in samples previously incubated with DCFH-DA: no CPNs and no light, with CPNs and no light and no CPNs and light. Additionally, a positive control experiment was performed by incubating the cells with H_2O_2 100 µM.

Evaluation of cell death mechanism

In an early stage of apoptosis, the phospholipid bilayer of the plasma membrane breaks up and exposes phosphatidylserine on its outer side. The exposure of phosphatidylserine is a hallmark of apoptosis and can be quantified using the fluorescent probe FITC-Annexin V (FITC) [47]. On the other hand, necrosis can be tested using propidium iodide (PI) staining. Cells (10^5 cells/ml) were seeded into 35 mm culture dishes overnight to a subconfluent state (80% confluency). Then, cells were incubated with CPNs (12 mg/l) for 24 h and irradiated (10 J/cm^2). Three negative control experiments were performed: no CPNs and no light, with CPNs and no light and no CPNs and light. 6 and 24 h after the PDT treatment, cells from each condition were centrifuged, washed with PBS and suspended in binding buffer (0.1 ml). Then, 5 µl of Annexin V-FITC (0.5 mg/ml) and 5 µl of PI solutions were added to each cell suspension and incubated for 15 min at room temperature in the dark according to the manufacturer's protocol (FITC Annexin V Apoptosis Detection Kit II Sigma-Aldrich Ltd., USA). The samples were finally analyzed on Millipore Guava easycyte 6 2L cytometer and data were processed with InCyte 3.1 software (GuavaSoft 3.1.1). Two independent experiments were performed (with n = 2 for each experiment).

Results & discussion

Formation & stability of CPNs

Particles were prepared as described in the experimental section. The hydrophobic interactions between F8BT chains, polystyrene backbones and PtOEP units produce densely packed CPNs in which the CPs and the porphyrin are in close contact. Considering the excellent solubility of polyethylene oxide in water [48] most PEG-COOH side chains are expected to be extended toward the aqueous solution [49]. CPNs suspended in growth medium supplemented with FBS showed excellent colloidal stability, no precipitates were observed even after several days, presumably because PEG-COOH side chains minimize nonspecific interactions with serum proteins. This characteristic is important for *in vivo* applications where particle stability in blood serum is a requirement, for example, when intravenous administration is desirable. Given the good colloidal stability of our particles, all experiments involving cells were done with CPNs suspended in culture media supplemented with FBS.

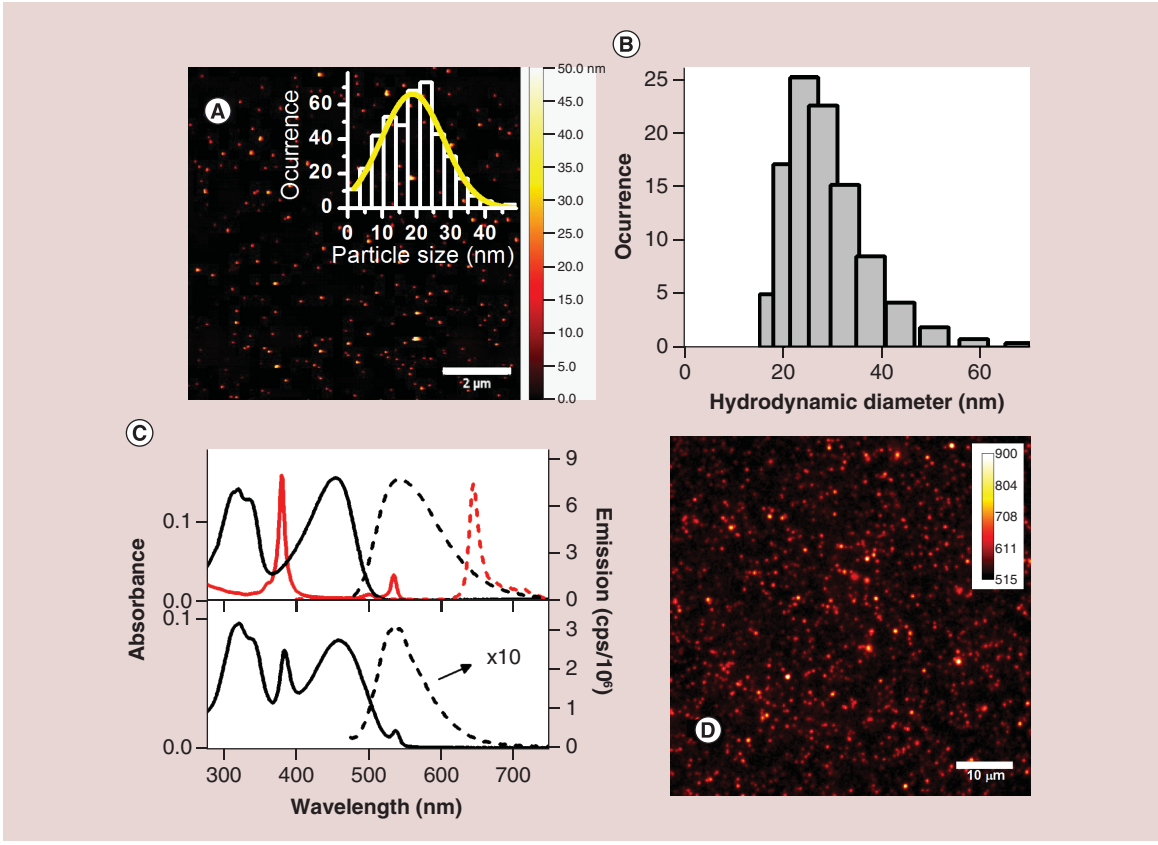

Figure 2. CPN characterization. (A) AFM image of CPNs over mica substrate, the false color height scale on the right is in nm. Insert: CPNs height distribution measured by AFM. **(B)** Hydrodynamic diameter histogram obtained by DLS of CPNs suspended in water. **(C)** Top panel: absorption (solid lines, left axis) and emission (dashed lines, right axis) spectra of F8BT (black) and PtOEP (red) in deoxygenated THF. Emission spectra were collected with excitation at 455 and 380 nm for F8BT (black) and PtOEP (red), respectively. Bottom Panel: absorption (solid line) and emission (dashed line) spectra of CPNs suspended in deoxygenated water. Emission spectrum was collected with excitation at 460 nm. All solutions were deoxygenated by Ar bubbling for 15 min before measurements. **(D)** Fluorescence micrograph of CPNs deposited over a clean coverslip. Emission intensity scale shown in false color.

CPNs size & spectral characterization

Water suspensions of CPNs were deposited over clean mica substrates as described in the experimental section and particle heights were measured using AFM. Figure 2A shows an AFM image of CPNs deposited over mica and the insert shows the size distribution of particles (bars) which can be well fitted with a Gaussian function (yellow curve) having a mean height of 19 nm and a standard deviation of 9 nm. Figure 2B shows the hydrodynamic diameter distribution measured by DLS of CPNs suspended in water having a mean hydrodynamic diameter of ~28 nm. The lack of agreement between AFM and DLS results can be rationalized considering that particle height measured over mica surfaces might not be equivalent to its diameter due to potential deformations induced by particle-mica interactions. More importantly, hydrodynamic diameters for these particles are expected to be larger than particle heights measured in dry conditions due to the formation of an extended particle solvation shell consisting of water molecules strongly interacting with extended PEG-COOH chains. Figure 2C bottom panel shows the absorption (solid line) and emission (dashed line) spectra of CPNs suspended in deoxygenated water. Figure 2C top panel shows the absorption (solid line) and emission (dashed line) of F8BT (black line) and PtOEP (red line) in deoxygenated THF. PtOEP emission corresponds to the phosphorescence of its triplet excited state (^{3}PtOEP*). Comparison of top and bottom panels indicates that in CPNs the absorption peaks at 384 nm and 537 nm correspond to the Soret and Q bands of PtOEP, respectively; whereas the peak at 460 nm corresponds to F8BT. PtOEP aggregation has been previously observed in polystyrene (and other polymer matrixes) at 10% w/w doping and it was evidenced by the appearance of a new absorption peak at ~412 nm [50]. Such peak is not observed in the absorption of

10.2217/nnm-2017-0292

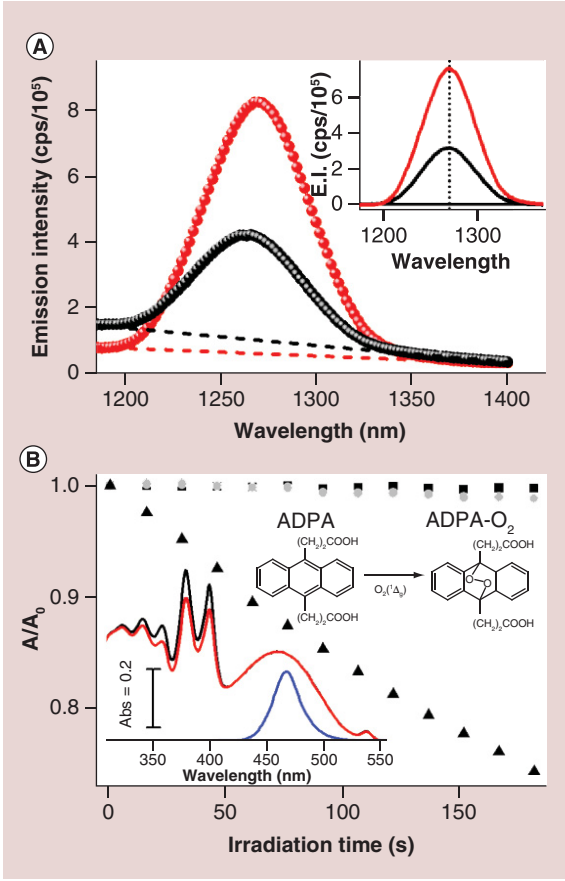

Figure 3. Evaluation of $O_2(^1\Delta_g)$ generation. (A) Steady-state emission spectrum in the NIR region generated by Eosin Y (red dots) and CPNs (black dots) in aerated D_2O solutions. Fluorescence emission backgrounds are shown as dashed lines. Inset: $O_2(^1\Delta_g)$ emission spectrum obtained by subtraction of the sample signals and the corresponding fluorescence backgrounds. The vertical dotted line shows the emission maximum at ~1268 nm. **(B)** CPNs photosensitized ADPA consumption/oxidation as a function of irradiation time in the presence of air monitored at 400 nm (triangles, see text for details). Absorption changes during irradiation monitored at 460 (squares) and 535 nm (circles) mainly associated with F8BT and PtOEP absorption, respectively, are also shown for comparison. Top Insert: ADPA oxidation by $O_2(^1\Delta_g)$. Bottom insert: Absorption spectra of the ADPA solution (~3.3 × 10^{-5} M) in presence of CPNs at 0 s (black) and 180 s (red) irradiation time with a blue led (blue line).

our CPNs suggesting no evidence for the formation of porphyrin aggregates within the particles. Similar results were observed in previous work from our group with particles containing F8BT and PtOEP (up to 10% w/w) but without PS-PEG-COOH [51]. The emission spectrum of CPNs in aqueous suspension is similar in shape to that of F8BT in THF and no PtOEP emission was observed. The lack of PtOEP emission in a similar system and under analogous conditions was previously assigned to efficient quenching of the emissive ^{3}PtOEP* state by energy transfer to the CPs to generate the triplet excited state of F8BT (^{3}F8BT*) (*vide infra*) [51]. The Figure 2D shows an emission micrograph of a sample prepared by deposition of a CPNs suspension in water on clean glass coverslip through spincasting. Bright emission spots observed in the image are assigned to F8BT fluorescence (see dashed line in Figure 2C bottom panel) from individual CPNs. Overall, the results confirm that the method used in the synthesis allows obtaining particles with the following characteristics: nanometric dimensions, relatively narrow size distribution and detectable at the single particle level using fluorescence microscopy [52].

$O_2(^1\Delta_g)$ phosphorescence measurements

Direct evidence for the formation of $O_2(^1\Delta_g)$ upon irradiation of nanoparticles in D_2O was obtained by steady state near infrared (NIR) emission spectroscopy. These measurements allow to determine directly the presence of $O_2(^1\Delta_g)$ by detecting its characteristic phosphorescence in the NIR spectral range (maximum at ~1268 nm) [53]. Figure 3A shows the $O_2(^1\Delta_g)$ steady state emission spectrum of a CPNs in D_2O solutions upon excitation at 487 nm. The fluorescence background signals (dashed lines) were obtained from similar experiments in Ar saturated solutions. Relative Φ_Δ were estimated by comparing the phosphorescence intensity of the CPNs sample with that of Eosin Y. From these experiments, a value of $\Phi_\Delta \sim 0.24$ was obtained for CPNs in excellent agreement with that previously reported for very similar particles [51]. In this earlier work a unique mechanism was proposed for the photogeneration of $O_2(^1\Delta_g)$ that differs from those previously described for analogous free-base porphyrin-doped CPNs [33,54]. Briefly, the excited singlet state of F8BT (^{1}F8BT*) is generated upon selective photoexcitation. Intraparticle exciton migration and subsequent singlet energy transfer from ^{1}F8BT* to the tetrapyrrole generates the excited singlet state of PtOEP (^{1}PtOEP*). Efficient intersystem crossing in the metallated porphyrin generates

quantitatively ^{3}PtOEP*. Later, ^{3}PtOEP* transfers triplet energy to the CP to generate ^{3}F8BT* which produces $O_2(^1\Delta_g)$. Thus, in this mechanism the combination of efficient light collection and energy transfer from F8BT to the porphyrin and induced high quantum yield of ^{3}F8BT* led to the 'amplified' generation of $O_2(^1\Delta_g)$. A more detailed description of this mechanism is provided in the supporting information.

Photooxidation of ADPA

To further explore the photosensitized formation of singlet oxygen from aqueous CPNs suspensions, photooxidation kinetic studies were performed adding ADPA in water, which is a well-known $O_2(^1\Delta_g)$ chemical trap. Figure 3B shows the consumption of ADPA in the presence of CPNs (triangles) as a function of the irradiation time. Changes of ADPA concentration are fast in air saturated suspension whereas control experiments under the same conditions but in argon saturated suspensions (not shown) show negligible ADPA consumption. ADPA concentration changes in the presence of O_2 are associated with the photosensitized production of $O_2(^1\Delta_g)$ by the CPNs and subsequent oxidation of ADPA to give the corresponding endoperoxide (ADPA-O_2, Figure 3B top insert). Further control experiments in the absence of CPNs (not shown) demonstrate that auto-photosensitization of ADPA is negligible under the experimental conditions due to the lack of significant overlap between ADPA absorption and blue LED emission (Figure 3B bottom insert, blue line). Thus we conclude that CPNs act as effective PS for the oxidation of ADPA and presumably for other organic/biological substrates. Figure 3B bottom insert shows the absorption spectra of ADPA in the presence of CPNs before (black line) and after irradiation for 180 s (red line). The spectrum of the nanoparticles remains unchanged after irradiation (compare black and red lines above 420 nm) suggesting that these particle sensitizers are resistant to ROS induced oxidation/degradation processes usually seen for conventional PS [55]. The lack of significant changes in the absorption of CPNs is further evidenced in the main panel of Figure 3A, where the absorption at 460 nm (squares) and 535 nm (circles) corresponding mainly to F8BT and PtOEP, respectively, are shown to be essentially constant during photoirradiation.

CPNs uptake & intracellular localization

Flow cytometry is a powerful and fast tool to analyze uptake of fluorescent particles by cells [30,56,57]. CPNs cellular uptake was observed in three different cell lines (Figure 4); two of them were tumor cell lines from colon (SW480) and brain (T98G) and the other one was a macrophage cell line (RAW 264.7). Cytometry experiments performed after CPNs (24 mg/l) incubation for 6 and 24 h with each cell line indicate that T98G (Figure 4A) and RAW 264.7 (Figure 4B) have significantly higher particle uptake as compared with SW480 (Figure 4C). Figure 4D shows that the percentage of cells that incorporated CPNs (after incubation for 24 h) is 77 ± 5, 70 ± 1 and 28 ± 2, for T98G, RAW 264.7 and SW480, respectively. Additional experiments performed as a function of particle incubation time (Figure 4E) indicate that T98G and RAW 264.7 cells continued to incorporate nanoparticles even at 24 h (maximum incubation time tested), whereas SW480 cells reached maximum particle incorporation at 6 h. Similar experiments aimed to asses particle uptake have been previously reported employing other CPNs on TE-71, MDA-MB-231, A549 and OVCAR3 cell lines [30]. The results of these experiments indicate particle uptake in all studied cell lines.

While flow cytometry experiments confirm the uptake of CPNs they do not provide information regarding particle distribution within cells. To investigate the intracellular localization of CPNs we took advantage of their intrinsic fluorescent properties (see Figure 2C). Particle distribution and colocalization with cell organelles was performed using confocal fluorescence microscopy. Figure 5 shows fluorescent micrographs of T98G (top row), RAW 264.7 (bottom row), SW480 (middle row) cells after incubation (24 h) with CPNs (12 mg/l). The images clearly show that all cell lines incorporate CPNs consistent with flow cytometry results. Confocal images of SW480 cells showed that most CPNs are localized on (or near) the cell membrane and only a low fraction of particles are distributed intracellularly (Supplementary Figure 1, see Supporting Information). This result is consistent with the low CPNs uptake by these cells evaluated by flow cytometry. Conversely, confocal fluorescence micrographs of T98G and RAW 264.7 cells showed a predominantly perinuclear distribution of CPNs and colocalization with lysosomes. It is well known that intracellular localization of PS affects cell death mechanisms triggered by PDT. Thus, colocalization analysis with CPNs and organelles was performed using the Pearson correlation coefficient (PCC) (Supplementary Figure 2, see Supporting Information). These results indicate that CPNs colocalized with lysosomes in T98G and RAW 264.7 with PCC of 0.60 ± 0.02 and 0.65 ± 0.02, respectively. In contrast, for SW480 PCC was much lower (0.28 ± 0.02) indicating less colocalization with these organelles. PCC obtained

10.2217/nnm-2017-0292

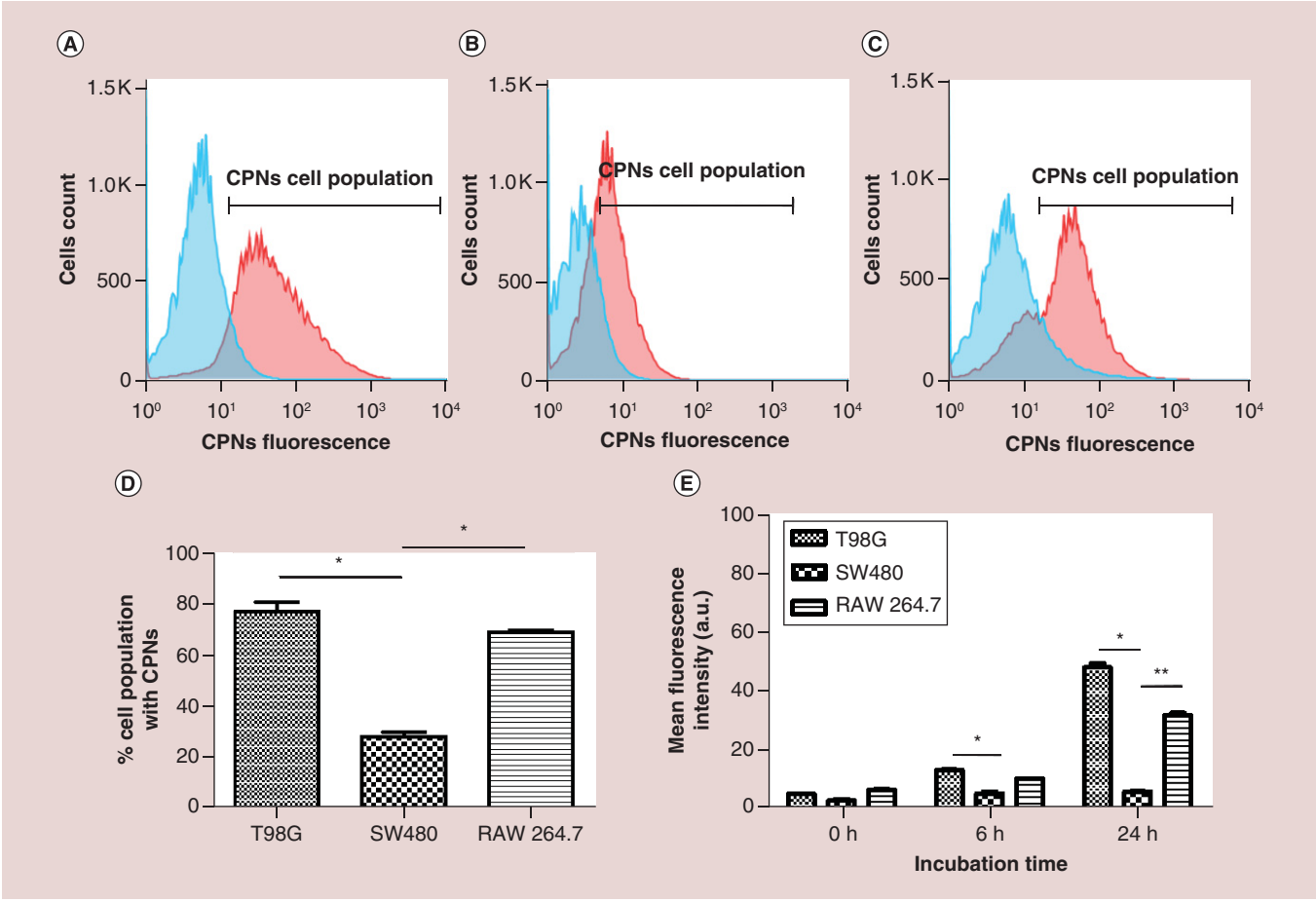

Figure 4. Uptake quantification of CPNs by flow cytometry of (A) T98G, (B) SW480 and (C) RAW 264.7 cell lines. Red curves represent cells incubated (24 h) with CPNs (24 mg/l) and blue curves represent controls (without particle incubation). **(D)** Percentage of the cell population showing CPNs uptake obtained from **(A, B & C)** histograms (see text for details), *$p < 0.001$ with ANOVA test. **(E)** CPNs cellular uptake as a function of incubation. Bar graph represents the geometric mean fluorescence intensity in the green channel of cell populations of two independent experiments, and 0 h represents the negative control group (without particle incubation), *$p < 0.01$ and **$p < 0.001$ with ANOVA test. All incubation experiments were performed at 37°C.

for correlation between localization of CPNs and mitochondrias or actin filaments were much lower indicating no colocalization with these cell structures.

The observed lysosome colocalization suggests an endocytic mechanism of particle uptake in our experiments which is consistent with previous reports for CPN incorporation in different cell lines [58,59]. Haimov *et al.* reported an active, temperature dependent, mechanism for the incorporation of PS doped CPNs into MCF-7 tumor cells [60]. Additionally, Fernando *et al.* confirmed an endocytic mechanism for CPN uptake in macrophages with final particle localization in lysosomes [61]. In that work it was concluded that particle uptake occurred via constitutive macropinocytosis (rather than clathrin-dependent or caveolin-dependent mechanisms). On the other hand, increased levels of macropinocytosis can be a beneficial nutrient uptake mechanism to support proliferation of cancer cells [62] and tumor development. Considering this background information particle uptake in our experiments might be mediated by macropinocytosis.

Biocompatibility of CPNs in macrophages & tumor cells

In order to evaluate the intrinsic cytotoxicity of CPNs in the studied cell lines a colorimetric cell viability assay was implemented. To this purpose, mitochondrial MTT reduction assay was performed as an index of cytotoxicity. No cell mortality in the dark was observed for all the cell lines incubated with each CPNs concentration up to 48 h (Supplementary Figure 3, see Supporting Information). Moreover, overall cell morphology did not change for all cell lines when comparing CPNs incubated cells with control cells (Figure 6 upper and middle rows).

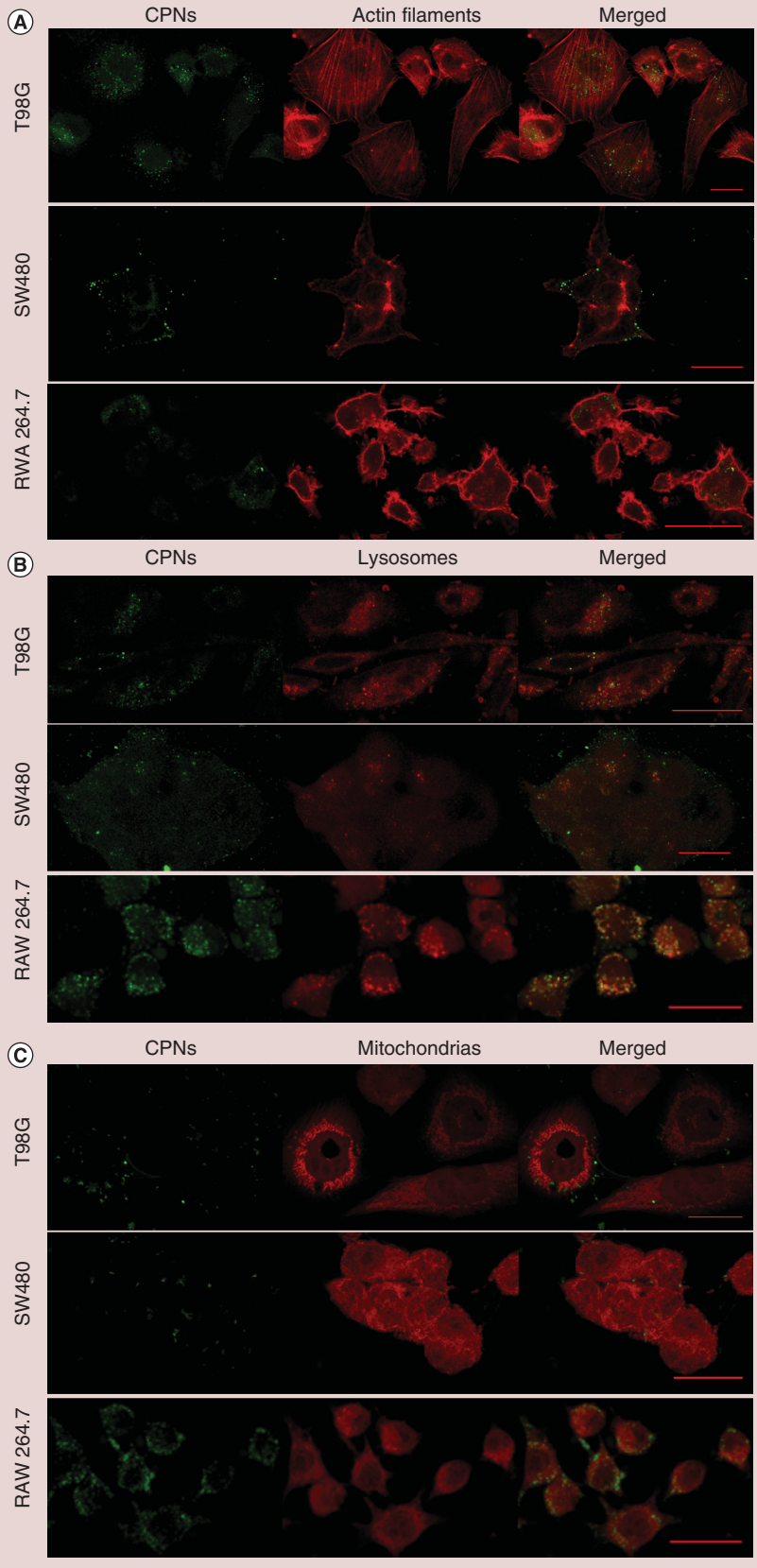

Figure 5. CPN intracellular distribution. Confocal fluorescence images obtained from the middle plane of cells showing CPNs (green channel) into T98G, SW480 and RAW 264.7 and **(A)** actin filaments (red channel), **(B)** lysosomes (red channel) and **(C)** mitochondria (red channel). Merged images showed yellow overlap with lysosomes mainly. Scale bar = 200 μm.

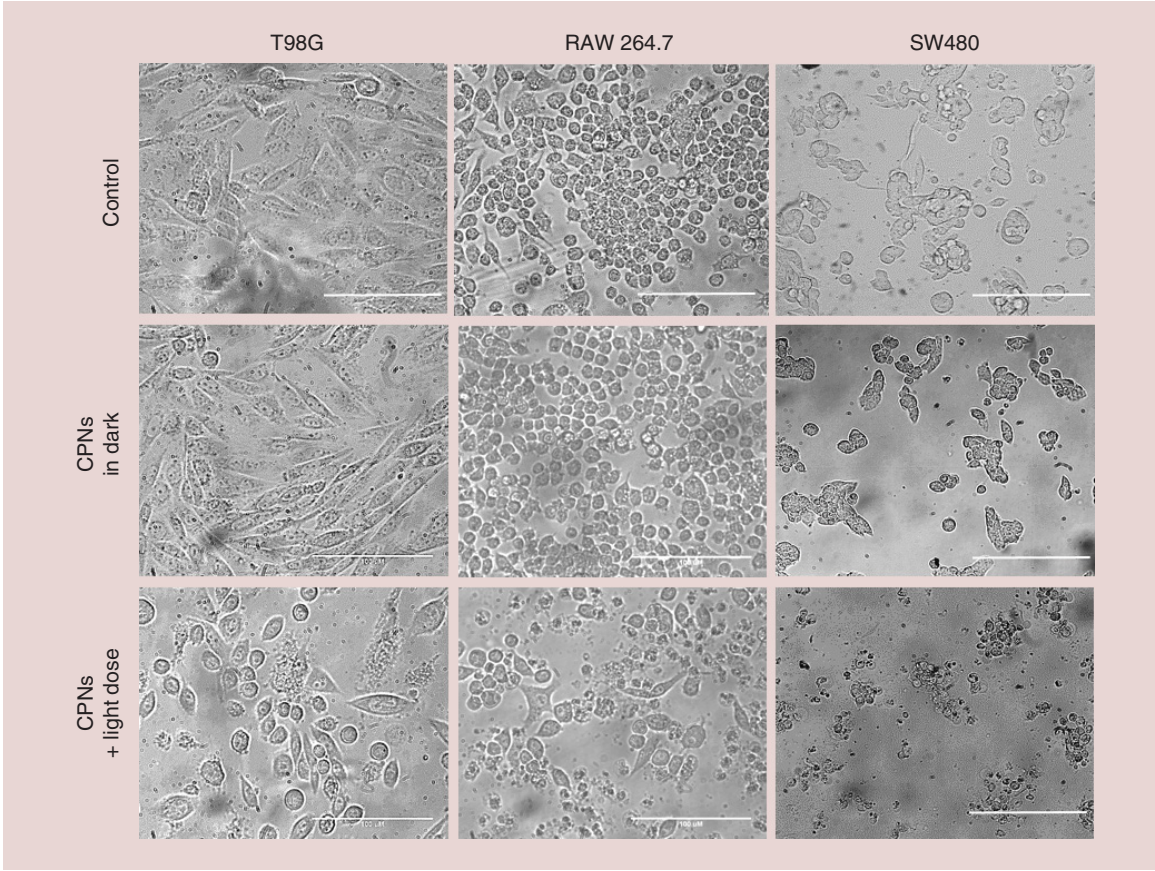

Figure 6. Cell morphology after PDT with CPNs. Brightfield images of cell lines obtained in an inverted optical microscope corresponding to treatment with CPNs 24 mg/l during 24 h (in dark) and 24 h after PDT with CPNs 24 mg/l and 10 J/cm^2 light dose compared with control cells without any treatment (light or CPNs exposure). Scale bar = 100 μM

Viability results using mitochondrial MTT reduction were further confirmed by morphological analysis of stained nuclei (Supplementary Figure 6, Supporting Information) and by FITC/PI cellular staining monitored by flow cytometry. These results are in agreement with previous biocompatibility reports of CPNs in various cancer cell lines at different exposure times [30,31,36,60,63,64]. Once it was verified that the incorporation of CPNs did not affect the normal functioning of T98G, RAW 264.7 and SW480 cells, the phototherapeutic effect of the particles was investigated.

PDT using CPNs

Figure 7 shows the viability of the studied cell lines incubated with various concentrations of CPNs and irradiated with different light doses. Cells not incubated with CPNs were viable at all light doses employed, whereas a significant toxic effect was found in all cell lines after PDT. The table shown in Figure 7D collects the IC_{50} values estimated from graphs a-c. IC_{50} values for RAW 264.7 and SW480 are similar at all used light doses and are significantly lower than those obtained for T98G cells. These results highlight the inherent PTD susceptibility of each cell line, which depends on several factors such as degree of cellular uptake, intracellular localization of PS and/or different ROS-scavenging mechanisms. The PDT effect was also evident in brightfield images of treated cells which showed changes in cell phenotype with apoptotic appearance, cell detachment and debris (Figure 6, bottom row). Intuitively, the efficiency of a PS can be related to the doses of PS and light required to achieve cell death; the lower the doses the higher the efficiency. However, to be able to strictly compare PS efficiencies a common protocol must be followed. Unfortunately, such a standardized procedure for PDT experiments is rarely found in the literature, even for *in vitro* experiments, making the comparison of PS efficiencies practically impossible. As

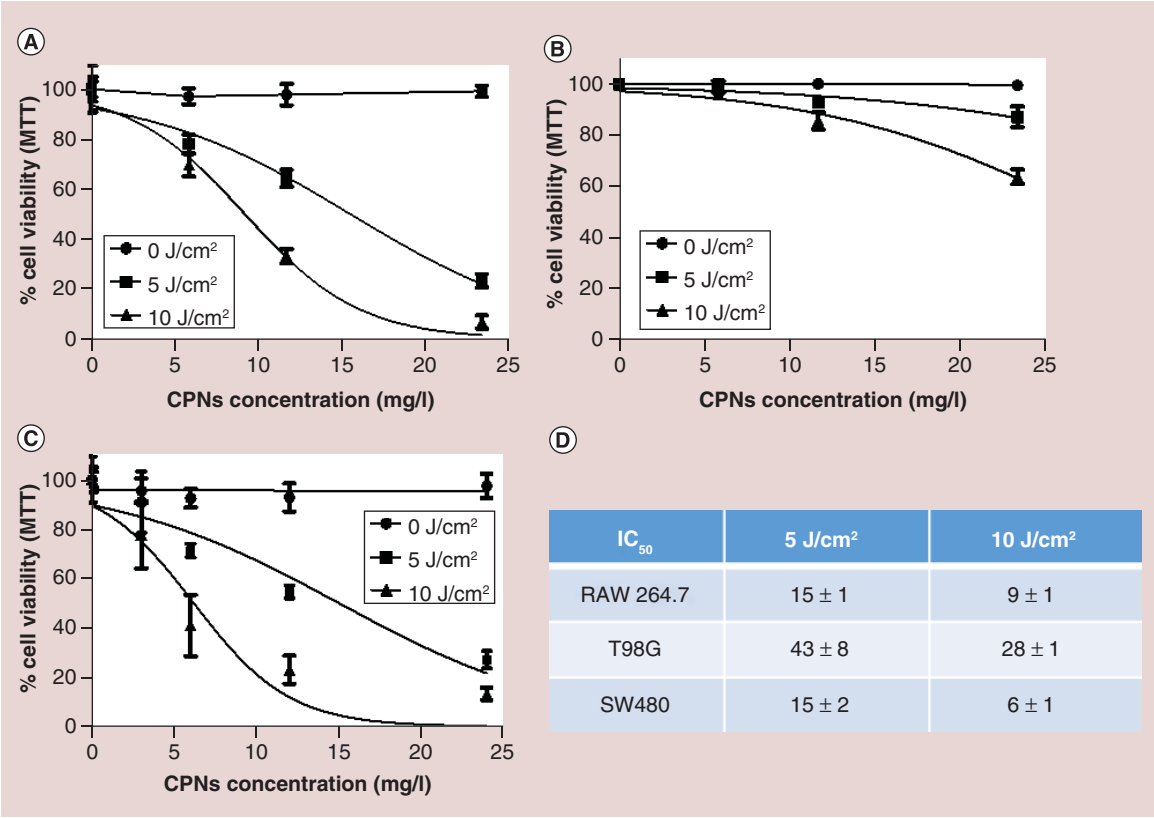

IC_{50}	5 J/cm²	10 J/cm²
RAW 264.7	15 ± 1	9 ± 1
T98G	43 ± 8	28 ± 1
SW480	15 ± 2	6 ± 1

Figure 7. Cell viability (quantified by MTT assay 24 h after PDT) for (A) RAW 264.7, (B) T98G and (C) SW480 cell lines as a function of CPN concentration during incubation and light dose. (D) Table indicating the inhibitory concentration estimated to affect cell viability by 50 % (IC_{50}) expressed in mg/l for each cell line and irradiation dose. IC_{50} values were obtained by nonlinear regression fitting (lines) to the MTT results (data points) shown in **(A–C)** with GraphPad Prism 5 software.

mentioned before, we followed the EN ISO 10993–5 protocol for particle incubation and viability quantification which clearly define the conditions in our PTD experiments.

To our knowledge, this is the first report of CPNs PDT in colorectal and brain tumor cells. Additionally, we observed efficient PDT effect in macrophages which are an important component of the tumor microenvironment. These cells play a predominant role in progression of several solid tumors (like brain and CRC) and therefore have been used as therapeutic targets [65,66]. As mentioned before, photostable PS are highly desirable for PDT. Further evidence for the excellent photostability of our CPNs is obtained from the fluorescence and brightfield images shown in Supplementary Figure 4. Fluorescence micrographs demonstrate that CPNs emission intensity does not change significantly upon PDT, whereas brightfield micrographs show considerable morphological changes consistent with cell death after treatment.

Cellular oxidative stress

The capacity of CPNs to induce oxidative stress in the dark (intrinsic cytotoxicity) and upon light irradiation was tested with DCFH-DA as described in the Materials and methods section. As shown in Figure 8 (first row) upon irradiation of T98G (A columns) and SW480 (B columns) cells, previously incubated with CPNs, a prominent green florescence is observed indicating elevated levels of intracellular oxidative stress. As was shown previously CPNs efficiently produce $^1O_2$ upon irradiation, it is well known that in the intracellular environment this excited oxygen species can produce peroxides that induce cell death. Control experiments performed in the dark show very week fluorescence indicating negligible production of intracellular ROS, even at the highest CPNs concentrations used (Figure 8, second row). Analogous results were obtained in control experiments including light treatment but without CPNs (Figure 8, third row). A positive control experiment incorporating H_2O_2 in the dark shows intense intracellular fluorescence signals (Figure 8, fourth row) confirming the probe's good performance. These combined

10.2217/nnm-2017-0292

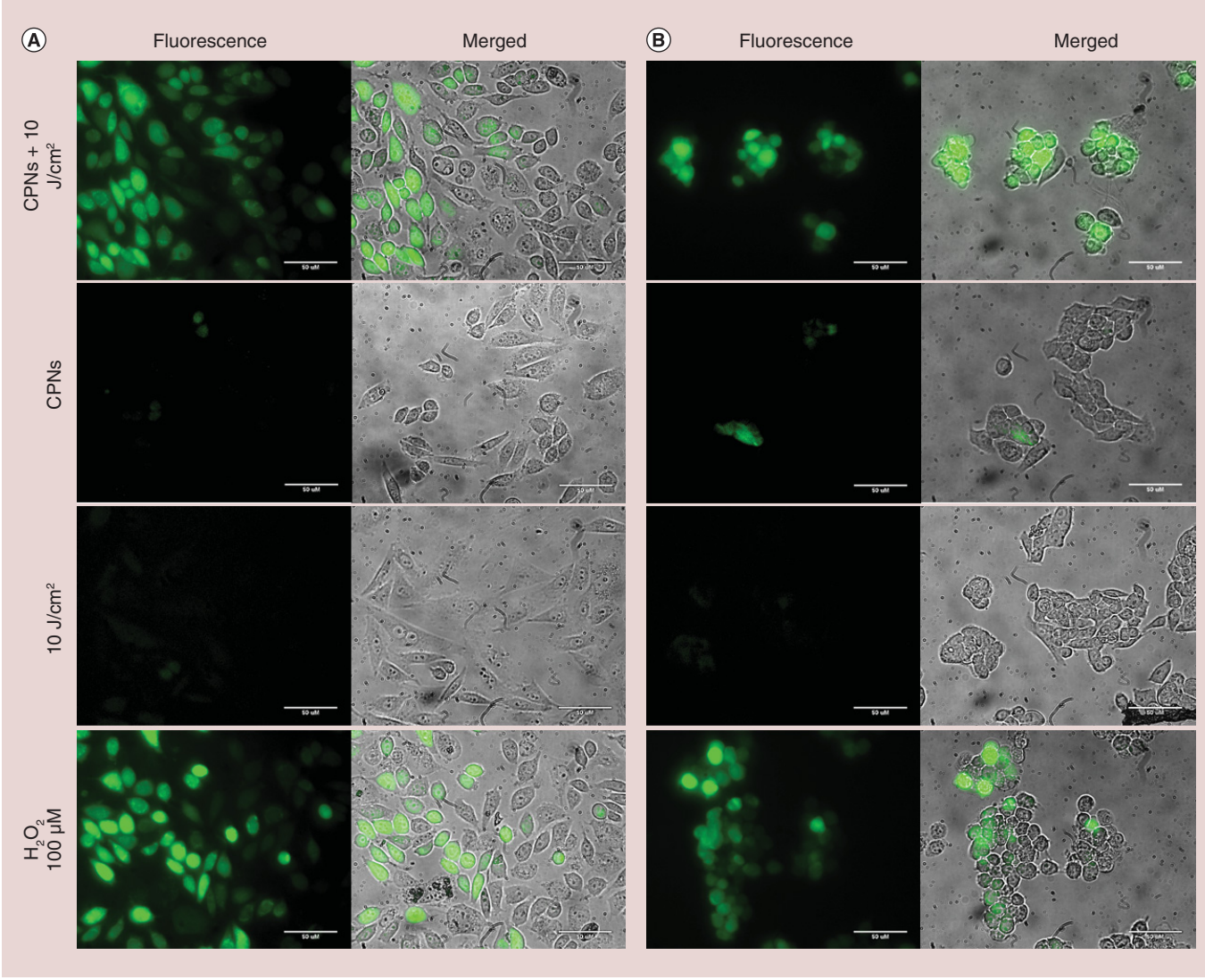

Figure 8. Detection of ROS generated after PDT in (A) T98G and (B) SW480 cell lines. CPNs + 10 J/cm^2 row represents treatment with 24 mg/l CPNs and light dose 10 J/cm^2 immediately post irradiation. CPNs row represents cells incubated with 24 mg/l (no light) indicating no ROS production by CPNs exposure. 10 J/cm^2 row represents cells irradiated treated with 10 J/cm^2 (no CPNs) indicating no photocytotoxicity is observed. H_2O_2 100 μM row represents a control positive of cells incubated with hydrogen peroxide 100 μM (no CPNs, no light). The green fluorescence corresponds to DCF-DA dye oxidized due to the presence of ROS. Scale bar = 50 μM

results are consistent with the previously discussed viability experiments and suggest that, in our PDT protocol, oxidative stress is the main mechanism for cellular damage leading to cell death. Similar results, in which intracellular ROS were detected upon sensitizer irradiation, have been reported employing other CPs nanoparticles [31,63]. Our results provide further evidence for the key role of ROS-induced cell damage in PDT using CPNs.

Cell death mechanism

The mechanisms of cell death induced by PDT were tested using an FITC Annexin V Apoptosis Detection Kit II as described in the experimental section. Double staining of cells with FITC and PI monitored by flow cytometry allows discrimination of: live (FITC-/PI-), early apoptotic (FITC+/PI-), late apoptotic (FITC+/PI+) and necrotic (FITC-/PI+) cells. Late apoptotic signals (FITC+/PI+) are presumably due to loss of membrane integrity and PI permeation at the latest stages of apoptosis [67,68]. As shown in Figure 9 column A, the incubation of cells with CPNs in absence of light did not induce cell death (live cells > 90 %) in any of the studied cell lines consistent with previously shown MTT viability assays. Additional control experiments with: cells without particle incubation and

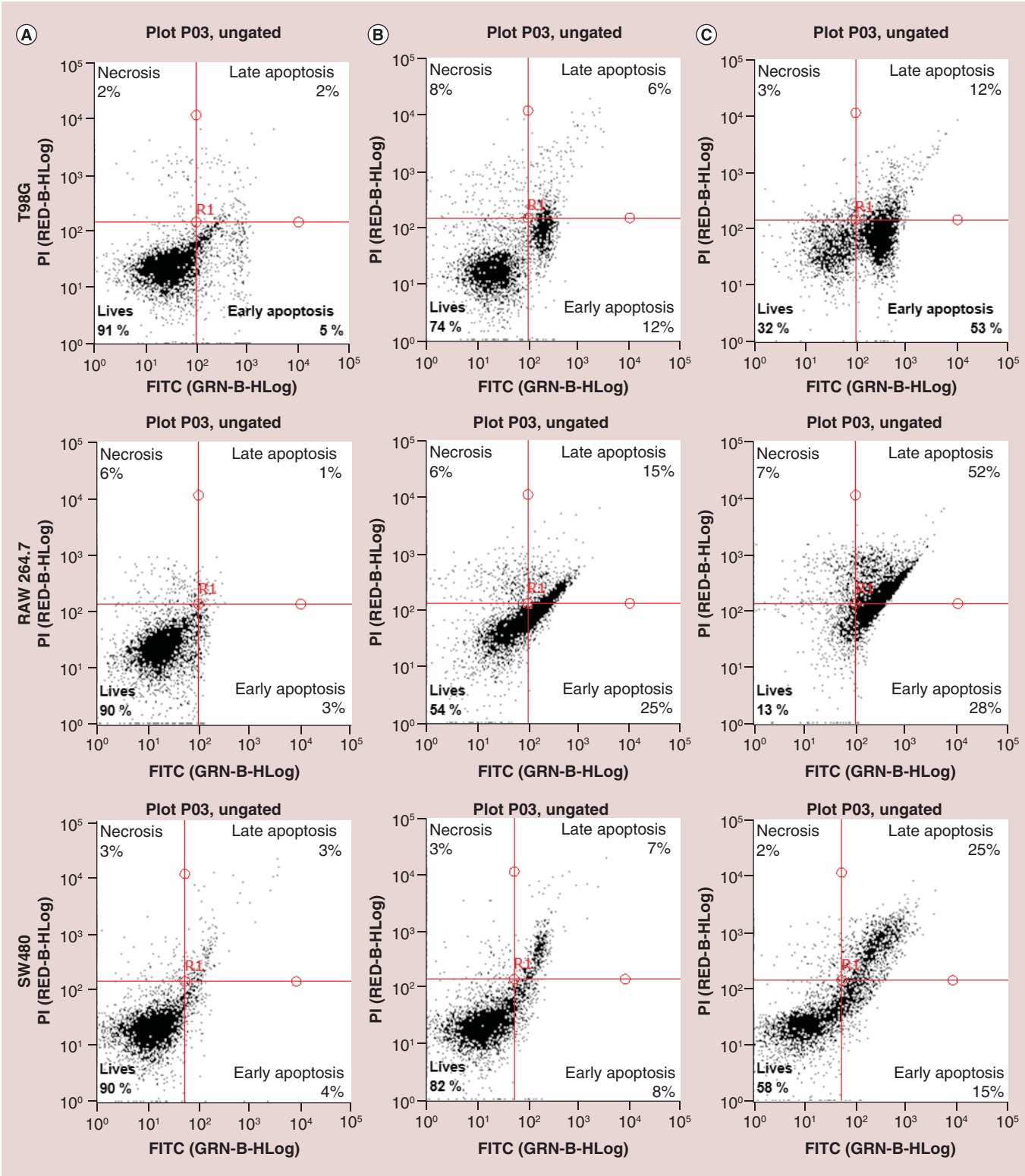

Figure 9. Flow cytometry experiments to test apoptosis (FITC+) versus necrosis (PI+). Column **(A)** corresponds to CPNs 12 mg/l treatment without light in T98G, RAW 264.7 and SW480 cells. Column **(B & C)** correspond to 6 h and 24 h post PDT treatment (12 mg/l CPNs, 10 J/cm^2), respectively, in T98G, RAW 264.7 and SW480.

10.2217/nnm-2017-0292

not exposed to light and cells without particle incubation but irradiated; show that live cells (FITC-/PI-) are more than 97 % of the total cell population (see Supplementary Figure 5). On the other hand, cells monitored 6 and 24 h after PDT treatment showed variable degrees and types of cell death (Figure 9, column B & C). For T98G cells the predominant mechanism of PDT induced death is apoptosis. As seen in Figure 9 top row, the percentage of apoptotic T98G cells increases from 12 to 53 when samples are monitored at 6 and 24 h after PDT, respectively; whereas the degree of late apoptosis is relatively minor. On the other hand, RAW 264.7 and SW480 cells showed a larger fraction of late apoptotic cells at all tested times after PDT, as compared with T98G cells. It is important to note that performing these flow cytometry experiments at two (or more) waiting periods after PDT treatment allows to evaluate the kinetic evolution of the labeling process to better assign the apoptotic nature of FITC+/PI+ cells. To further test that PDT induces apoptosis, membrane permeation and nuclear morphology was examined using PI and Hoechst 33258 staining, respectively. Results are shown in the Supporting Information (Supplementary Figure 6). At 24 hours after PDT, cells stained with PI (+) also show nuclear features such as chromatin condensation and apoptotic bodies. These results suggest that apoptosis is indeed the main death mechanism for cells labeled as FITC-/PI+ in the cytometry experiments. The poor agreement between live cell percentages obtained by the FITC Annexin V/PI assay and MTT experiments can be rationalized considering that these methods are based on monitoring different cell events (linked to cell death) occurring in different time scales upon PDT. Additionally, the mechanisms (and kinetics) of the detection methods are also different. The combination of these factors necessarily yields dissimilar cell viability values for the two methods at a given time [69]. Overall, our results provide strong evidence linking apoptosis with cell damage caused by CPs nanoparticles in PDT protocols.

Conclusion

In summary, we prepared metallated (Pt)-porphyrin doped CPNs stabilized through PS-PEG chains with suitable size and colloidal stability for PDT treatment of cancerous cells. The ability of these CPNs to photogenerate $^1O_2$ ($\Phi_\Delta = 0.24$) in water was confirmed by monitoring the NIR $^1O_2$ emission. Additionally, colloidal stability and biocompatibility in brain and CRC tumor cell lines and normal cells were confirmed. Cell uptake and intracellular localization studies showed that the particles are well incorporated into glioblastoma and macrophages cells with a final localization in lysosomes. Conversely, CRC cells were less efficient incorporating CPNs and the final particle localization seems to be the plasmatic membrane. A PDT protocol using the prepared CPNs was tested for the *in vitro* killing of the previously mentioned cell lines. This treatment was efficient inducing oxidative stress that triggered cell apoptosis as the main mechanism of cell death. The relatively low doses of PS ($IC_{50} = 6–28$ mg/l) and light (10 J/cm^2) necessary to achieve death of 50% of cell population in our experiments results from the extremely high particle absorption cross-section and reasonable quantum yield of $^1O_2$ generation. To our knowledge, this is the first report of effective PDT treatment of macrophages, colorectal and brain tumor cells using CPNs as PS. As mentioned before, macrophages play a chief role in tumor development and therefore can be used as therapeutic targets.

Future perspective

CPNs represent a revolution for the development of new photosensitizer agents providing a suitable platform for light-based cancer theranostics procedures. However, accurate preclinical trials to evaluate their pharmacokinetics and *in vivo* tumor specific anticancer activity are still required to confirm the full potential of these particles.

Acknowledgements

Authors acknowledge financial support of this work by Agencia Nacional de Promoción Científica y Tecnológica (ANPCyT)-Argentina, Instituto Nacional del Cancer-Argentina, Consejo Nacional de Investigaciones Científicas y Técnicas (CONICET)-Argentina and Secretaría de Ciencia y Técnica (SECyT)- Universidad Nacional de Río Cuarto (UNRC)-Argentina. L.P.M., G.V.P., C.L, C.A.C., V.A.R. and R.E.P. are permanent research staff of CONICET. L.E.I. thanks CONICET for a postdoctoral scholarship. R.M.S. and R.A.P thank CONICET for PhD scholarships.

Financial & competing interests disclosure

This work was supported by CONICET (grant numbers: PIP 11220150100069 and 11220150100295/2015), ANPCyT (grant numbers: PICT 1439/13, 914/14 and 214/14), Instituto Nacional del Cancer (grant number: 1006/2016) and SECyT-UNRC (grant number: PPI 2016 18/6487). The authors have no other relevant affiliations or financial involvement with any organization or entity with a financial interest in or financial conflict with the subject matter or materials discussed in the manuscript apart from those disclosed.

Summary points

Synthesis of nanoparticle photosensitizer based on conjugated polymers

- The prepared particles consisted of a conjugated polymer matrix doped with metallated porphyrin and having PEG stabilizing side chains (conjugated polymer nanoparticles [CPNs]).
- CPNs show small size (mean diameter ~ 28 nm) and narrow size distribution.
- CPNs are colloidally stable even in growth medium supplemented with FBS after several days.

$O_2(^1\Delta_g)$ generation photosensitized by CPNs

- The combination of efficient light collection and energy transfer from 9,9-dioctylfluorene-*alt*-benzothiadiazole to the porphyrin induced high quantum yield of ^{3}F8BT* that led to the 'amplified' generation of $O_2(^1\Delta_g)$.
- Photooxidation of a model polycyclic aromatic hydrocarbon by CPNs is highly efficient.

CPNs uptake & biocompatibility in colorectal & brain tumor cells & macrophages

- T98G and RAW 264.7 cell lines showed significantly higher particle uptake as compared with SW480 with a final localization of CPNs into lysosomes due to an endocytic entry.
- Upon CPNs exposure (in the dark) no cell mortality was observed at different particle concentrations and endpoint times highlighting the biocompatibility of the CPNs.

PDT using CPNs kills cancerous cells & macrophages through an apoptotic pathway

- An efficient PDT effect was achieved with very low light doses in all studied cell lines.
- CPNs show excellent photostabilty under PDT conditions.
- PDT treatment promoted intracellular ROS generation as tested by DCFH-DA.
- The predominant mechanism of death trigger by PDT was apoptosis in all studied cell lines.

No writing assistance was utilized in the production of this manuscript.

Supplementary data

To view the supplementary data that accompany this paper please visit the journal website at: www.futuremedicine.com/doi/full/10.2217/nnm-2017-0292

References

Papers of special note have been highlighted as: • of interest; •• of considerable interest

1 Li L, Huh KM. Polymeric nanocarrier systems for photodynamic therapy. *Biomater. Res.* 18, 19 (2014).

2 Milla Sanabria L, Rodríguez ME, Cogno IS *et al.* Direct and indirect photodynamic therapy effects on the cellular and molecular components of the tumor microenvironment. *Biochim. Biophys. Acta.* 1835(1), 36–45 (2013).

• **Reviews the direct and indirect (through alterations of tumor microenvironment) effects of photodynamic therapy (PDT) on cancer cells.**

3 Huang Z. A review of progress in clinical photodynamic therapy. *Technol. Cancer Res. Treat.* 4(3), 283–293 (2005).

4 Mannino S, Molinari A, Sabatino G *et al.* Intratumoral vs systemic administration of meta-tetrahydroxyphenylchlorin for photodynamic therapy of malignant gliomas: assessment of uptake and spatial distribution in c6 rat glioma model. *Int. J. Immunopathol. Pharmacol.* 21(1), 227–231 (2008).

5 Matsumura H, Akimoto J, Haraoka J, Aizawa K. Uptake and retention of the photosensitizer mono-l-asparthyl chlorine e6 in experimental malignant glioma. *Lasers Med. Sci.* 23(3), 237–245 (2008).

6 Namatame H, Akimoto J, Matsumura H, Haraoka J, Aizawa K. Photodynamic therapy of C6-implanted glioma cells in the rat brain employing second-generation photosensitizer talaporfin sodium. *Photodiagnosis Photodyn. Ther.* 5(3), 198–209 (2008).

7 AKIMOTO J. Photodynamic Therapy for Malignant Brain Tumors. *Neurol. Med. Chir. (Tokyo).* 56(4), 151–157 (2016).

• **Reviews the state-of-the-art PDT for primary malignant brain tumors. Highlights the pioneering role of the Japanese government in approving PDT for cancer treatment in humans for the first time in the world.**

8 Zavadskaya TS. Photodynamic therapy in the treatment of glioma. *Exp. Oncol.* 37(4), 234–241 (2015).

9 Kawczyk-Krupka A, Bugaj AM, Latos W, Zaremba K, Wawrzyniec K, Sieroń A. Photodynamic therapy in colorectal cancer treatment: the state of the art in clinical trials. *Photodiagnosis Photodyn. Ther.* 12(3), 545–553 (2015).

• **Gives a general overview of the PDT application to colorectal cancer in the field of clinical trials to emphasize its curative, and insufficiently exploited potential.**

10 Kawczyk-Krupka A, Bugaj AM, Latos W *et al.* Photodynamic therapy in colorectal cancer treatment – the state of the art in preclinical research. *Photodiagnosis Photodyn. Ther.* 13, 158–174 (2016).

11 Robertson CA, Evans DH, Abrahamse H. Photodynamic therapy (PDT): a short review on cellular mechanisms and cancer research applications for PDT. *J. Photochem. Photobiol. B.* 96(1), 1–8 (2009).

12 Mroz P, Yaroslavsky A, Kharkwal GB, Hamblin MR. Cell death pathways in photodynamic therapy of cancer. *Cancers (Basel)* 3(2), 2516–2539 (2011).

13 Castano AP, Demidova TN, Hamblin MR *et al.* Mechanisms in photodynamic therapy: part two-cellular signaling, cell metabolism and modes of cell death. *Photodiagnosis Photodyn. Ther.* 2(1), 1–23 (2005).

14 Rumie Vittar NB, Lamberti MJ, Pansa MF *et al.* Ecological photodynamic therapy: new trend to disrupt the intricate networks within tumor ecosystem. *Biochim. Biophys. Acta* 1835(1), 86–99 (2013).

15 Lucky SS, Soo KC, Zhang Y. Nanoparticles in photodynamic therapy. *Chem. Rev.* 115(4), 1990–2042 (2015).

16 Debele TA, Peng S, Tsai HC. Drug carrier for photodynamic cancer therapy. *Int. J. Mol. Sci.* 16(9), 22094–22136 (2015).

17 Achyuthan KE, Bergstedt TS, Chen L *et al.* Fluorescence superquenching of conjugated polyelectrolytes: applications for biosensing and drug discovery. *J. Mater. Chem.* 15(27–28), 2648 (2005).

18 Xing C, Xu Q, Tang H, Liu L, Wang S. Conjugated polymer/porphyrin complexes for efficient energy transfer and improving light-activated antibacterial activity. *J. Am. Chem. Soc.* 131(36), 13117–13124 (2009).

19 Tian Z, Yu J, Wu C, Szymanski C, McNeill J. Amplified energy transfer in conjugated polymer nanoparticle tags and sensors. *Nanoscale* 2(10), 1999–2011 (2010).

20 Szymanski C, Wu C, Hooper J *et al.* Single molecule nanoparticles of the conjugated polymer MEH-PPV, preparation and characterization by near-field scanning optical microscopy. *J. Phys. Chem. B.* 109(18), 8543–8546 (2005).

•• **The first report refers to the development of conjugated polymer nanoparticles (CPNs) in aqueous medium with suitable size and fluorescence properties.**

21 Wu C, Bull B, Szymanski C, Christensen K, McNeill J. Multicolor conjugated polymer dots for biological fluorescence imaging. *ACS Nano.* 2(11), 2415–2423 (2008).

•• **Highly fluorescent CPNs were developed for biological purpose and CPNs based on 9,9-dioctylfluorene-altbenzothiadiazole serve to label macrophages for the first time.**

22 Feng X, Lv F, Liu L *et al.* Conjugated polymer nanoparticles for drug delivery and imaging. *ACS Appl. Mater. Interfaces* 2(8), 2429–2435 (2010).

23 Li S, Jiang X-F, Xu Q-H. Polyfluorene based conjugated polymer nanoparticles for two-photon live cell imaging. *Sci. China Chem.* 1–9 (2017).

24 Lan M, Zhao S, Xie Y *et al.* Water-soluble polythiophene for two-photon excitation fluorescence imaging and photodynamic therapy of cancer. *ACS Appl. Mater. Interfaces.* 9(17), 14590–14595 (2017).

25 Feng G, Liu J, Liu R, Mao D, Tomczak N, Liu B. Ultrasmall conjugated polymer nanoparticles with high specificity for targeted cancer cell imaging. *Adv. Sci.* 4(9), 1600407 (2016).

26 Li K, Liu B. Polymer-encapsulated organic nanoparticles for fluorescence and photoacoustic imaging. *Chem. Soc. Rev.* 43(18), 6570–6597 (2014).

27 Li Y, Liu J, Liu B, Tomczak N. Highly emissive PEG-encapsulated conjugated polymer nanoparticles. *Nanoscale* 4(18), 5694 (2012).

28 Pecher J, Huber J, Winterhalder M, Zumbusch A, Mecking S. Tailor-made conjugated polymer nanoparticles for multicolor and multiphoton cell imaging. *Biomacromolecules.* 11(10), 2776–2780 (2010).

29 Wu C, Szymanski C, Mcneill J. Preparation and encapsulation of highly fluorescent conjugated polymer nanoparticles. *Langmuir* (27), 2956–2960 (2006).

30 Doshi M, Copik A, Gesquiere AJ. Development and characterization of conducting polymer nanoparticles for photodynamic therapy *in vitro*. *Photodiagnosis Photodyn. Ther.* 12(3), 476–489 (2015).

•• **An extensive *in vitro* PDT study where CPNs are highly effective at moderate light doses mainly in OVCAR 3 cells.**

31 Doshi M, Krienke M, Khederzadeh S *et al.* Conducting polymer nanoparticles for targeted cancer therapy. *RSC Adv.* 5(47), 37943–37956 (2015).

32 Bhattacharyya S, Barman MK, Baidya A, Patra A. Singlet oxygen generation from polymer nanoparticles-photosensitizer conjugates using FRET cascade. *J. Phys. Chem. C.* 118(18), 9733–9740 (2014).

33 Chang K, Tang Y, Fang X, Yin S, Xu H, Wu C. Incorporation of porphyrin to ??-conjugated backbone for polymer-dot-sensitized photodynamic therapy. *Biomacromolecules* 17(6), 2128–2136 (2016).

34 Dmitriev RI, Borisov SM, Düssmann H *et al.* Versatile conjugated polymer nanoparticles for high-resolution O2 imaging in cells and 3D tissue models. *ACS Nano.* 9(5), 5275–5288 (2015).

35 Shen X, Li L, Min Chan AC, Gao N, Yao SQ, Xu QH. Water-soluble conjugated polymers for simultaneous two-photon cell imaging and two-photon photodynamic therapy. *Adv. Opt. Mater.* 1(1), 92–99 (2013).

36 Shen X, Li S, Li L, Yao SQ, Xu QH. Highly efficient, conjugated-polymer-based nano-photosensitizers for selectively targeted two-photon photodynamic therapy and imaging of cancer cells. *Chemistry* 21(5), 2214–2221 (2015).

37 Mehraban N, Freeman H. Developments in PDT sensitizers for increased selectivity and singlet oxygen production. *Materials (Basel)* 8(7), 4421–4456 (2015).

38 Grimland JL, Wu C, Ramoutar RR, Brumaghim JL, McNeill J. Photosensitizer-doped conjugated polymer nanoparticles with high cross-sections for one- and two-photon excitation. *Nanoscale.* 3(4), 1451–1455 (2011).

•• **The first report of development of phorphyrin doped CPNs for potential application in PDT.**

39 Bilski P, Dabestani R, Chignell CF. Influence of cationic surfactant on the photoprocesses of eosine and rose bengal in aqueous solution. *J. Phys. Chem.* 95(15), 5784–5791 (1991).

40 Lindig BA, Rodgers MAJ, Schaap AP. Determination of the lifetime of singlet oxygen in water-d2 using 9,10-anthracenedipropionic acid, a water-soluble probe. *J. Am. Chem. Soc.* 102(17), 5590–5593 (1980).

41 Schmidt R, Schaffner K, Trost W, Brauer HD. Wavelength-dependent and dual photochemistry of the endoperoxides of anthracene and 9,10-dimethylanthracene. *J. Phys. Chem.* 88(5), 956–958 (1984).

42 Nečas D, Klapetek P. Gwyddion: an open-source software for SPM data analysis. *Open Phys.* 10(1), 181–188 (2012).

43 Ponzio RA, Marcato YL, Gómez ML, Waiman CV, Chesta CA, Palacios RE. Crosslinked polymer nanoparticles containing single conjugated polymer chains. *Methods Appl. Fluoresc.* 5(2), 24001 (2017).

44 Dunn KW, Kamocka MM, McDonald JH. A practical guide to evaluating colocalization in biological microscopy. *AJP Cell Physiol.* 300(4), C723–C742 (2011).

45 Bolte S, Cordelières FP. A guided tour into subcellular colocalization analysis in light microscopy. *J. Microsc.* 224(3), 213–232 (2006).

46 Royall JA, Ischiropoulos H. Evaluation of 2′,7′-dichlorofluorescin and dihydrorhodamine 123 as fluorescent probes for intracellular H_2O_2 in cultured endothelial cells. *Arch. Biochem. Biophys.* 302(2), 348–355 (1993).

47 AshaRani PV, Low Kah Mun G, Hande MP, Valiyaveettil S. Cytotoxicity and genotoxicity of silver nanoparticles in human cells. *ACS Nano.* 3(2), 279–290 (2009).

48 Mishra P, Nayak B, Dey RK. PEGylation in anti-cancer therapy: an overview. *Asian J. Pharm. Sci.* 11(3), 337–348 (2016).

49 Wu C, Schneider T, Zeigler M *et al.* Bioconjugation of ultrabright semiconducting polymer dots for specific cellular targeting. *J. Am. Chem. Soc.* 132(43), 15410–15417 (2010).

50 Nifiatis F, Su W, Haley JE, Slagle JE, Cooper TM. Comparison of the photophysical properties of a planar, PtOEP, and a nonplanar, PtOETPP, porphyrin in solution and doped films. *J. Phys. Chem. A.* 115(47), 13764–13772 (2011).

51 Spada RM, Macor LP, Hernández LI *et al.* Amplified singlet oxygen generation in metallated-porphyrin doped conjugated polymer nanoparticles. *Dye. Pigment.* 149, 212–223 (2018).

•• **A detailed study of the photophysics and the mechanism of improvement singlet oxygen $O_2(^1\Delta_g)$ generation of PtoEP-doped CPNs.**

52 Jiménez Banzo AM. New insights in photodynamic therapy: production, diffusion and reactivity of singlet oxygen in biological systems. Doctoral thesis, Universitat Ramon Llull, Barcelona, Spain (2008). http://hdl.handle.net/10803/9310

53 Khan AU, Kasha M. Direct spectroscopic observation of singlet oxygen emission at 1268 nm excited by sensitizing dyes of biological interest in liquid solution. *Proc. Natl Acad. Sci. USA* 76(12), 6047–6049 (1979).

54 Shen X, Li L, Wu H, Yao SQ, Xu Q-H. Photosensitizer-doped conjugated polymer nanoparticles for simultaneous two-photon imaging and two-photon photodynamic therapy in living cells. *Nanoscale* 3(12), 5140 (2011).

55 Bonnett R, Martínez G. Photobleaching of sensitisers used in photodynamic therapy. *Tetrahedron* 57(47), 9513–9547 (2001).

56 Peñaloza JP, Márquez-Miranda V, Cabaña-Brunod M *et al.* Intracellular trafficking and cellular uptake mechanism of PHBV nanoparticles for targeted delivery in epithelial cell lines. *J. Nanobiotechnol.* 15(1), 1 (2017).

57 Han Y, Li X, Chen H *et al.* Real-time imaging of endocytosis and intracellular trafficking of semiconducting polymer dots. *ACS Appl. Mater. Interfaces.* 9(25), 21200–21208 (2017).

58 Shen X, Li L, Wu H, Yao SQ, Xu Q-H. Photosensitizer-doped conjugated polymer nanoparticles for simultaneous two-photon imaging and two-photon photodynamic therapy in living cells. *Nanoscale* 3(12), 5140–5146 (2011).

59 Li S, Shen X, Li L *et al.* Conjugated-polymer-based red-emitting nanoparticles for two-photon excitation cell imaging with high contrast. *Langmuir* 30(26), 7623–7627 (2014).

•• **The mode of entry of CPNs in cells was comparable to other small molecules and nanomaterials been lysosomes the final destination.**

60 Haimov E, Weitman H, Ickowicz D, Malik Z, Ehrenberg B. Pdot nanoparticles attach photosensitizers non-covalently and enhance efficiently the photodynamic effect by FRET. *RSC Adv.* 5, 18482–18491 (2015).

61 Fernando LP, Kandel PK, Yu J, McNeill J, Ackroyd PC, Christensen KA. Mechanism of cellular uptake of highly fluorescent conjugated polymer nanoparticles. *Biomacromolecules* 11(10), 2675–2682 (2010).

62 Commisso C, Davidson SM, Soydaner-Azeloglu RG *et al.* Macropinocytosis of protein is an amino acid supply route in Ras-transformed cells. *Nature* 497(7451), 633–637 (2013).

63 Feng L, Zhu J, Wang Z. Biological functionalization of conjugated polymer nanoparticles for targeted imaging and photodynamic killing of tumor cells. *ACS Appl. Mater. Interfaces.* 8(30), 19364–19370 (2016).

64 Tang Y, Chen H, Chang K *et al.* Photo-cross-linkable polymer dots with stable sensitizer loading and amplified singlet oxygen generation for photodynamic therapy. *ACS Appl. Mater. Interfaces.* 9(4), 3419–3431 (2017).

65 Vinogradov S, Warren G, Wei X. Macrophages associated with tumors as potential targets and therapeutic intermediates. *Nanomedicine* 9, 695–707 (2014).

66 Hayashi N, Kataoka H, Yano S *et al.* A novel Photodynamic therapy targeting cancer cells and tumor-associated macrophages. *Mol. Cancer Ther.* 14(2), 452–460 (2014).

67 Zhao L, Su R, Cui W, Shi Y, Liu L, Su C. Preparation of biocompatible heat-labile enterotoxin subunit B-bovine serum albumin nanoparticles for improving tumor-targeted drug delivery via heat-labile enterotoxin subunit B mediation. *Int. J. Nanomed.* 9, 2149 (2014).

68 Hong C, Lee J, Zheng H, Hong S-S, Lee C. Porous silicon nanoparticles for cancer photothermotherapy. *Nanoscale Res. Lett.* 6(1), 321 (2011).

69 Henslee EA, Torcal Serrano RM, Labeed FH *et al.* Accurate quantification of apoptosis progression and toxicity using a dielectrophoretic approach. *Analyst.* 141(23), 6408–6415 (2016).